Determination of the fracture toughness of a 9Cr ODS steel fuel cladding using the pin loading Tension test

B. Rais, J. Garnier, E. Pons, B. Marini, Jacques Besson

Determination of the Fracture Toughness of a 9Cr ODS steel fuel cladding using the Pin Loading Tension test.

B. Rais[1,2], J. Garnier[1], E. Pons[1], B. Marini[1] and J. Besson[2]

[1]*Université Paris-Saclay, CEA, Service de Recherches Matériaux et procédés Avancés, 91191, Gif-sur-Yvette, France*

[2] *MINES Paris, PSL Research University, Centre des Matériaux, CNRS UMR 7633, 91003 Evry, France*

ARTICLE INFO

Keywords :

fracture toughness

Pin Loading Tension test

ODS steel fuel cladding

Fracture resistance curve

ABSTRACT

A Pin Loading Tension (PLT) test was developed to evaluate the fracture behavior of thin-walled tubes. The fracture resistance curve ($J-R$ curve) was determined from the load-CMOD curve using the single specimen technique based on the elastic unloading method following the procedure described in the ASTM E1820-22e1 standard [1]. However, the standard does not provide the necessary functions, geometric function $f(a/W)$ and plastic factor η_{pl}, to apply the methodology to the PLT test. In this work, the geometric functions needed to evaluate the crack length from the unloading compliance, which allows to highlight effects not seen in the past and the elastic and plastic parts of the J-integral were determined using finite element analysis. Special care was taken to consider the effects of contact and friction between the test specimen and the loading device. The methodology was then applied to experimentally study the crack growth resistance of a 9Cr ODS (Oxide Dispersion Strengthened) steel tube, which is a candidate material for fuel claddings of future fast-neutron reactors.

1. Introduction

Fast neutron reactors offer better efficiency in the use of fuel and reduce radioactive waste. These improvements mean severe thermomechanical sollicitations for the reactors' components, especially for their fuel cladding. ODS (Oxide Dispersion Strengthened) steels are candidate materials for the fuel cladding in these reactors. These steels have been proven to have good tensile and creep resistance at the expected service temperatures [2]–[4]. However, one of the particularities of these high-strength alloys is their limited ductility. It is, therefore, essential to know their resistance to crack propagation to ensure the integrity of the fuel cladding and avoid radioactive contamination of the reactors' primary circuit. These claddings are thin-walled tubes : wall thickness of 0.5 mm and external diameter of 10.73 mm.They are obtained using a cold rolling process that induces significant microstructural modifications of the material. Therefore, assessing the material toughness in the final geometry of the cladding is mandatory. The ASTM E1820-22e1 standard provides guidelines for conducting tests on cracked specimens [1]. It is based on several functions to obtain the crack propagation resistance curve ($J-R$ curve) from the force-CMOD curve. When using the unloading compliance technique, the procedure allows determining the entire $J-R$ curve using a single specimen. The ASTM E1820-22e1 standard [1] can be applied to C(T), DC(T), and SE(B) specimens but cannot be straightforwardly applied to thin-walled parts as it is impossible to sample standard fracture specimens from the fuel claddings due to their geometry.

Estimating the toughness of fuel claddings in terms of Stress Intensity Factor (SIF) or J-Integral requires the design and fabrication of adapted experimental setups together with the associated procedure to process the experimental load-displacement curves. Some tests have been developed in the literature to assess the toughness of thin-walled tubes [5]–[9]. The assessment of fracture toughness of ODS steel tubes has been performed by Nitu et al. in terms of stress intensity factors [10] using the Pin Loading Tension test (PLT) proposed by Grigoriev et al. [5].

Nomenclature

$A_{pl}, a, a_{(i)}, a_0, a_f$	Plastic area under load-CMOD curve, crack length, crack length at ith unloading, initial crack length, final crack length
B, b, b_0	Specimen thickness (two times the wall thickness for PLT specimen), uncracked ligament, initial uncracked ligament
$CMOD, C, C_{(i)}, C(a/W), C(T)$	Crack Mouth Opening Displacement, Compliance, Compliance at ith unloading, Compliance function, Compact Tension specimen
$DC(T)$	Disc Compact Tension specimen
E, E', e	Young modulus, Effective Young modulus $E/(1-\nu^2)$ in plane strain and E in plane stress, EDM mandrel cutting gap
$f(a/W), \mathrm{F_L}$	Geometric function, Limit load (or maximum load)
$G(b/W)$	Terms function of crack length in the load separation theory of Ernst *et al.*
$H(V_{pl}/W)$	Term function of plastic displacement in the load separation theory of Ernst *et al.*
$J, J_{el}, J_{pl}, J_{0.2}, J_1, J_{IC}$	J-integral, elastic part of J-integral, plastic part of J-integral, J-integral at 0.2 mm of crack extension, J-integral at 1 mm of crack extension, Critical mode I J-integral.
$K_I, K_{J_{0.2}}, K_{IC}$	Stress intensity factor for mode I opening, Sterss intensity factor corresponding to $J_{0.2}$, Critical stress intensity factor
P	Load
R_{int}, R_{mand}	Internal radius of PLT specimen tube, Mandrel's radius
$S_{ij}, SE(B)$	Separation factor corresponding to (P_i/P_j) loads for different crack lengths at the same plastic opening displacement, Single Edge Notched Bend specimen
t	PLT specimen's wall thickness
u	Normalized compliance
V_{pl}	Plastic CMOD
W	PLT test specimen's width (Distance between the load line and the end of the specimen)
γ_{pl}	Crack propagation correction factor
Δa	Crack extension
ε_p	Plastic accumulated strain
η_{pl}	Plastic factor
ν	Poisson's ratio
$\sigma, \sigma_u, \sigma_{YS}, \sigma_Y$	Stress, Ultimate tensile strength, Yield Stress, Yield Stress and Ultimate tensile strength average

Sanyal et al. [11] also proposed multiple-specimen and single-specimen methods to evaluate the fracture toughness of Zircaloy fuel cladding in terms of J-integral using the PLT test. In their study, the single-specimen procedure was applied using the normalization method of the ASTM E1820-22e1 standard [1] to determine the $J-$R curve [1]. CEA PLT specimen has a different geometry compared to Zircaloy PLT specimens and ODS steel PLT specimens tested in literature (see Fig. 9). Geometric functions $f_k(a/W)$ and η_{pl} determined by the othors are not applicable to CEA PLT specimen. This requires determining adapted geometric functions.

Moreover, in previous works [10], a muti-specimen method was used and only elastic part of the fracture toughness was determined on ODS steel fuel claddings. A new procedure based on the elastic unloading technique is proposed in this paper to determine the fracture toughness of thin-walled tubes.This new procedure uses the PLT test proposed by Grigoriev et al. [5]. Section 2 recalls the ASTM E1820-22e1 standard [1] procedure to determine $J-$R curves using the unloading compliance technique. Section 3 details the material and the testing apparatus used in this study. In section 4, the geometric parameters required to process the experimental data to obtain the $J-$R curve are evaluated using the Finite Element Method (FEM). A comparison of different methods proposed on literature and adapted to determine theses parameters for PLT specimen are detailed and compared. Section 5 exposes and discusses the experimental $J-$R curves obtained by the developed procedure on a 9Cr ODS steel tube, before concluding in section 6.

2. Procedure for the determination of $J-$R curves using the unloading compliance method

The analytical procedure for evaluating fracture toughness of materials in terms of J-integral from a single specimen is described in the ASTM E1820-22e1 standard [1]. The primary method recommended by the standard is the unloading compliance method. This method consists of performing elastic unloading cycles during the test and evaluating the instantaneous compliance $C_{(i)}$ (Fig. 1). This compliance allows estimating the instantaneous crack length $a_{(i)}$ and determining $J-$R curve from a single specimen. An alternative method was also proposed and referred to as "the normalization method". This method allows the determination of the intermediate crack lengths, without measuring them, from the normalized load, the initial crack length and the final crack length.

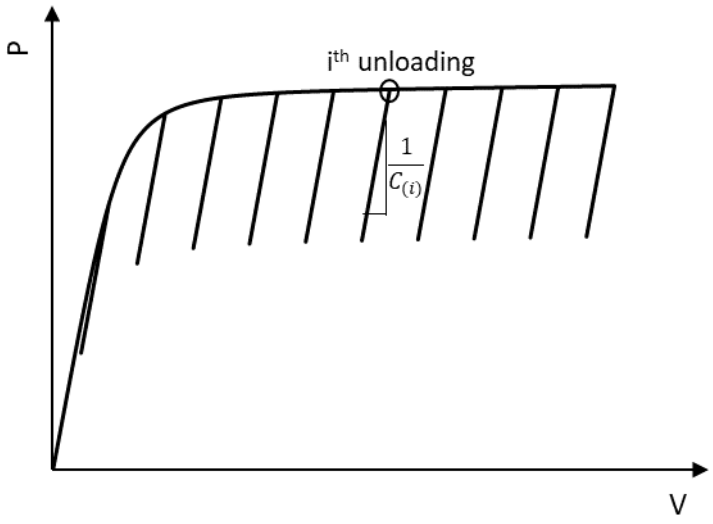

Fig. 1. Exemple of a load-CMOD curve with partial unloading and determination of elastic compliance

Under Mode I loading, the J-integral is expressed as the sum of an elastic part, J_{el}, and a plastic part, J_{pl}, as:

$$J = J_{el} + J_{pl} \tag{1}$$

This additive decomposition is strictly valid if the load applied to the cracked structure can be expressed as the product of a function depending on the crack length and a function of the plastic displacement [12]. The elastic part, J_{el}, is given by:

$$J_{el} = \frac{K_I^2}{E'} \quad (2)$$

Where $E' = E$ for plane stress, which is the case in this paper regarding the small thickness of the studied tubes, and $E/(1-\nu^2)$ for plane strain. E and ν are the Young's modulus and the Poisson's ratio, respectively. The mode I stress intensity factor K_I is defined as:

$$K_I = \frac{P}{B\sqrt{W}} f\left(\frac{a}{W}\right) \quad (3)$$

Where P is the applied load, B the specimen thickness, W the specimen width and $f(a/W)$ a function given by the ASTM E1820-22e1 procedure for standard specimens. $f(a/W)$ has to be defined for the nonstandard PLT specimen geometry. For a non-propagating crack, the relation between J_{pl} and the macroscopic plastic work is given as [13]:

$$J_{pl} = \frac{\eta_{pl} A_{pl}}{B\, b_0} \quad (4)$$

where A_{pl} is the plastic area under the load-displacement curve, B is the specimen thickness, used as it is when the specimen does not have Side Grooves like for PLT specimen, b_0 is the initial uncracked ligament ($b_0 = W - a_0$ where a_0 is the initial crack length and W is the specimen width). η_{pl} is a factor that is also geometry dependent but assumed independent of loading and which relates the plastic work to J_{pl}. It also needs to be determined for the PLT specimens. When the crack grows, the area under the load-displacement curve differs from the corresponding one for a non-propagating crack. Then, to determine J_{pl}, a correction for crack extension is needed, and equation (4) is not applicable [14]. The widely used procedure to evaluate J-integral, given in standards such as ASTM E1820-22e1, is the incremental procedure that evaluates J_{el} and J_{pl} at every applied elastic unloading point, denoted i, during the test (see Fig. 1). For $J_{el(i)}$, equation (2) is still valid using the current crack length ($a_{(i)}$) and the load corresponding to the i^{th} elastic unloading point ($P_{(i)}$) in equation (3). For J_{pl}, the measured load–displacement records must be corrected for crack extension to obtain an accurate estimation. Therefore, at i^{th} elastic unloading point from load-displacement curve measurement for growing crack J_{pl} is then defined as

$$J_{pl(i)} = \left(J_{pl(i-1)} + \frac{\eta_{pl(i-1)}}{b_{(i-1)}} \frac{A_{pl(i)} - A_{pl(i-1)}}{B}\right)\left(1 - \frac{\gamma_{(i-1)}}{b_{(i-1)}}\left(a_{(i)} - a_{(i-1)}\right)\right) \quad (5)$$

Where the correction factor $\gamma_{(i)}$ is given as:

$$\gamma_{(i)} = \eta_{pl(i)} - 1 - \frac{b_{(i)}}{W}\frac{\eta'_{pl(i)}}{\eta_{pl(i)}} \quad (6)$$

where η'_{pl} is the derivative of η_{pl} with respect to a/W.

The key ingredients for the experimental determination of the $J-$R curves are, therefore, the determination of the f and η_{pl} functions which are expressed as functions of a/W. The function relating compliance to crack length is also required. The ASTM E1820-22e1 standard [1] already provides these three functions for C(T), DC(T), and SE(B) specimens with some size limitations. The test must be performed in the range of $0.45 \leq a/W \leq 0.7$. The width of the specimen depends on its thickness, proportion ranges are $1 \leq W/B \leq 4$ for SE(B) specimen and $2 \leq W/B \leq 4$ for C(T) and DC(T) specimens. However, any thickness can be used as long as the qualification requirements are met. $f(a/W)$ and η_{pl} need to be determined in the case of PLT specimens, as detailed in section 4.

3. Material and experimental procedure

3.1. Material

The product studied in this work is a 1000 mm long tube manufactured by the french atomic energy agency, CEA, at the Nuclear Material Department.Its inner diameter is 9.73 mm with a wall thickness of 0.5 mm . The material is a 9Cr-

1W-0.3Ti-0.25Y_2O_3 (wt. %) martensitic ODS steel tube provided as the engineering tensile properties of the material are given in Table 1.

Table 1
Mechanical properties of CEA 9Cr ODS steel fuel cladding at room temperature

Property	Young's modulus (GPa) [15]	Poisson's ratio	Yield stress σ_{YS} (MPa)	UTS σ_u (MPa)	$\sigma_Y = 1/2\,(\sigma_{YS} + \sigma_u)$ (MPa)
Value	225	0.3	910	1026	968

This tube is manufactured using powder metallurgy. Hot extrusion is used for consolidation after mechanical alloying of a powder composed of a mixture of elementary powders composing the steel with a powder of yttrium oxide. The final shape is obtained by cold rolling with inter-pass heat treatments of austenitization at 1050°C for 15 min followed by a quench and a tempering at 750°C for 30 min. The microstructure of the 9% Cr ODS tube appears homogeneous in the thickness of the tube, according to the EBSD observations of the rolling plane (RD-ND) (Fig. 2-a) and transverse plane (ND-TD) (Fig. 2-b).

The microstructure shows grains of equiaxed shape with a diameter of about 1.2 µm. Some columnar grains along the rolling direction (RD) can be observed in the RD-ND section. This morphology is the heritage of the cold rolling process applied to obtain the final geometry. The analysis of the pole figures and orientation maps in both sections (see Fig. 2) shows a weakly textured microstructure with the presence of preferential crystallographic orientations, with an alignment of the <110> crystallographic axes of the grains parallel to the axial direction (RD) and <111> axes parallel to the normal direction (ND). This texture, generated by the rolling process, is attenuated by inter-pass heat treatments and final tempering. This type of microstructure was already observed on martensitic ODS steels manufactured at CEA [2], [4], [16].

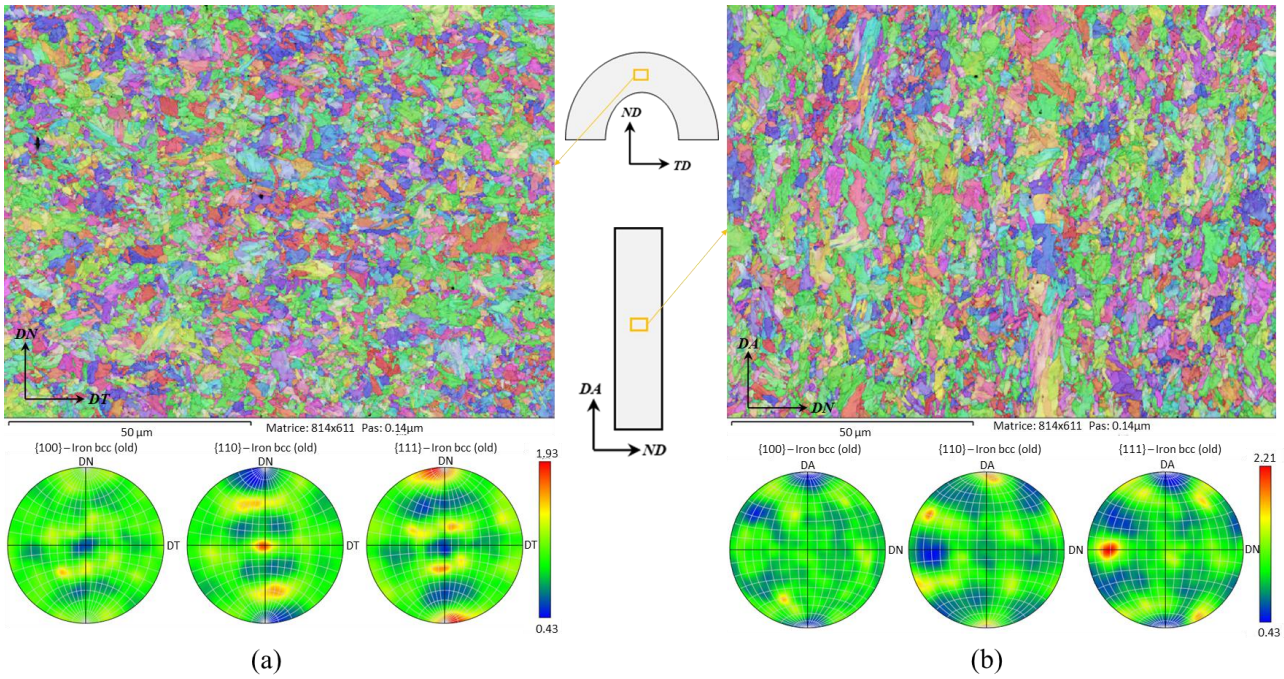

Fig. 2. EBSD Analysis of 9%Cr ODS Steel tube (a) Cross Section (b) longitudinal section

Recent ODS steels with a finer and more homogeneous precipitation have been developed at the CEA in the meantime. The average radius of YxTiyOz-type particles on these new ODS steels is of the order of a nanometer. This finer distribution of oxide particles is due to better control of the growth and coalescence kinetics of these precipitates during annealing [17], [18].

Particles of the same nature as nanometric oxide particles but with a stoichiometric composition Y2Ti2O7 with a radius between 5 and 50 nm were also observed by Sakasegawa et al. [19]. More recently, on more optimized alloys manufactured at the CEA, Sallez [20], Laurent-Brocq [21] as well as Hatzoglou [22] have observed these precipitates.

Other particles whose size can reach a few hundred nanometers are also present. These particles are considered undesirable because they weaken the material and promote its damage. These can be titanium oxides, carbides or nitrides [18]. Their presence is attributed to contamination during the preparation or mechanical alloying of the powders due to their presence at the grain boundaries [3], [19], [23], [24].

3.2. Specimen and setup configuration

Machining of the PLT specimen was performed using electro-discharge machining (EDM). The PLT specimen is a 17 mm long section of the tube. Two symmetric diametrically opposed notches were machined. The diameter of the notch root was 0.24 ± 0.01 mm (Fig. 3-b). Eleven PLT specimens with different machined notch lengths were fabricated. Specimens together with notch dimensions are referenced in Table 2. The loading setup consists of two half-cylinder mandrels inserted in the specimen (Fig. 3-a).

Two holes were machined at the end of the mandrel to insert the pins and load the specimens. The distance between the load line connecting the centers of the pin holes and the crack tip is denoted a and corresponds to the crack length. The distance between the load line and the end of the specimen was considered as the specimen effective width W and equals to 28.5 mm. It should be noted that the mandrels used to load the specimen behave as extensions of the specimen length so that W is larger than the height of the machined specimens. This is an interesting feature of the experimental setup in the case where the material is scarce (*e.g.*, irradiated material). Small extensions were machined at the bottom of the mandrels to attach a clip gauge used to measure crack opening displacement (CMOD) (see Fig. 3-a). The other end of the mandrels was machined to insert a pin (diameter: 3 mm). This pin defines a rotation axis for the mandrels and blocks the translation of the specimen along the mandrel's axis during loading. The nominal radius of the mandrels is 4.8 mm. After measuring it through optical microscopy, measurments gave a mandrel radius (R_{mand}) value of 4.8 ± 0.02 mm. The internal radius of the ODS steel tube (R_{int}) varies along his axis (± 30 µm). The difference between R_{int} and R_{mand} is noted Gap as shown in Fig. 3-c. The Gap values of every specimen are presented in Table 2. The mandrels were machined by cutting the full cylinder in two half-cylinders through EDM. This operation gived a second gap noted e of 0.3 mm at the initial position corresponding to the thickness of material removed during this cutting (see Fig. 3-c).

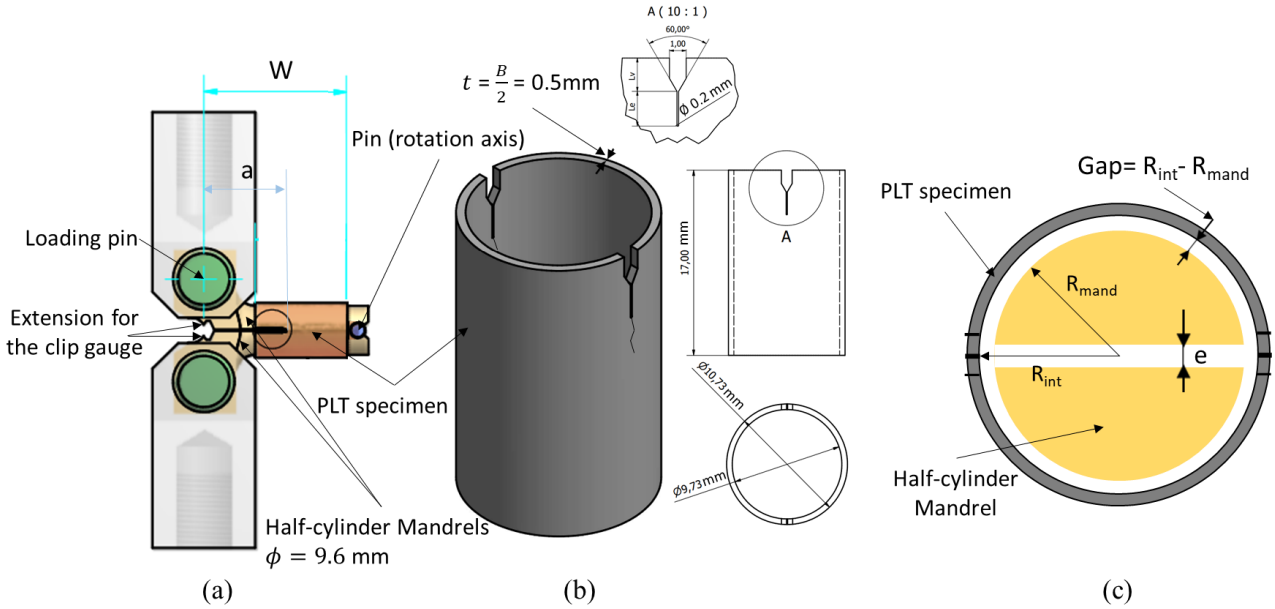

Fig. 3. Design of (a) loading fixture (b) PLT specimens (c) Side view of mandrels inserted in the PLT specimen (***Gap*** induced by ΔR between mandrel and internal surface of PLT specimen and ***e*** induced by EDM while separating the full cylinder in 2 halfs)

3.3. Pre-cracking and testing procedure

All the PLT specimens were subjected to fatigue loading to propagate a fatigue crack and perform fracture toughness tests on specimens with sharp cracks. Fatigue pre-cracking was performed using a 5kN servo-hydraulic machine. First, cycles with a maximum stress intensity factor $K_{\max}$ determined following equation (3) equal to 12 MPa$\sqrt{\text{m}}$ and an amplitude ΔK equal to 10 MPa$\sqrt{\text{m}}$ were applied and were decreased progressively down to about 8 MPa$\sqrt{\text{m}}$. $K_{\max}$ was chosen so that the plastic zone radius is negligible compared to the wall thickness and fatigue precracking deformations

does not interfere with toughness measurements. Fatigue crack extension was optically controlled every 3000 cycles to obtain the target crack lengths.

In some cases, differences in fatigue crack extensions at both notches exceeded 0.3 mm. The specimen was then rotated around the mandrel by 180° to reduce these différences. In addition, the crack front along the thickness was usually not straight. Fatigue crack extension was always larger at the inner surface of the specimen. FE simulations showed a significant stress gradient along the specimen thickness, which could explain why obtaining a straight front was difficult. In particular, opening stresses tended to be larger at the inner surface (see A.1).

Fracture toughness tests were conducted at room temperature on a 10 kN electro-mechanical testing machine. The CMOD was measured using a clip gauge. The loading program consisted of the following cycles: (i) loading at 0.1 mm/min until the CMOD increases by 0.03 mm, (ii) holding the CMOD for 60 s to allow for relaxation, (iii) unloading at 0.4 mm/min until 80% of load reached at the end of holding period, and (iv) reloading to 100% of this load at the same speed. The use of a relaxation period allows a better estimation of the unloading/loading compliance.

Table 2 Details of 3-point averaged post-fracture toughness testing measurements of initial crack lengths after fatigue pre-cracking (a_0) and final crack extensions (Δa)

Specimen reference	Notch lengths (mm)	Gap (µm)	a_0 after pre-cracking (mm)			Δa (mm)		
			Front side	Back side	Average	Front side	Back side	Average
Sp.1	2	59	15.190	14.990	15.090	1.913	2.363	2.138
Sp.2	4	40	17.134	17.052	17.093	2.128	1.312	1.720
Sp.3	4	36	17.006	17.263	17.135	1.903	2.940	2.422
Sp.4	5	43	17.310	16.917	17.114	5.077	3.308	4.193
Sp.5	6	59	18.274	18.927	18.601	1.743	2.528	2.136
Sp.6	6	40	18.019	18.381	18.200	2.624	3.261	2.943
Sp.7	7	50	19.165	19.663	19.414	1.754	2.453	2.104
Sp.8	7	32	19.172	19.093	19.133	2.721	3.954	3.338
Sp.9	7	63	19.455	19.031	19.243	2.305	3.622	2.964
Sp.10	8	44	20.045	20.359	20.202	2.577	4.356	3.467
Sp.11	8	51	20.029	20.067	20.048	2.525	4.220	3.373

3.4. Optical measurement of crack extension

To follow the crack extension during the test, a PCO.EDGE 5.5 camera equipped with a telecentric lens (magnification $\times 4$) was installed facing the specimen. The side observed with the camera is referred to as the front side; the other side is referred to as the back side. The observation area was 4.1×3.5 mm^2 and the pixel size was 1.6 µm. This direct method was used to determine the crack initiation point and measure crack extension during loading phases where the unloading compliance method is not applicable (see below). Specimens were break-open after testing by propagating the crack using the same setup until total failure of the specimen. It was done at -150 °C to highlight all the different cracking zones. The failed specimens were then observed with a Keyence optical microscope. 3D reconstructions of the cracked zones were made and crack extensions were measured from, as shown in Fig. 4.

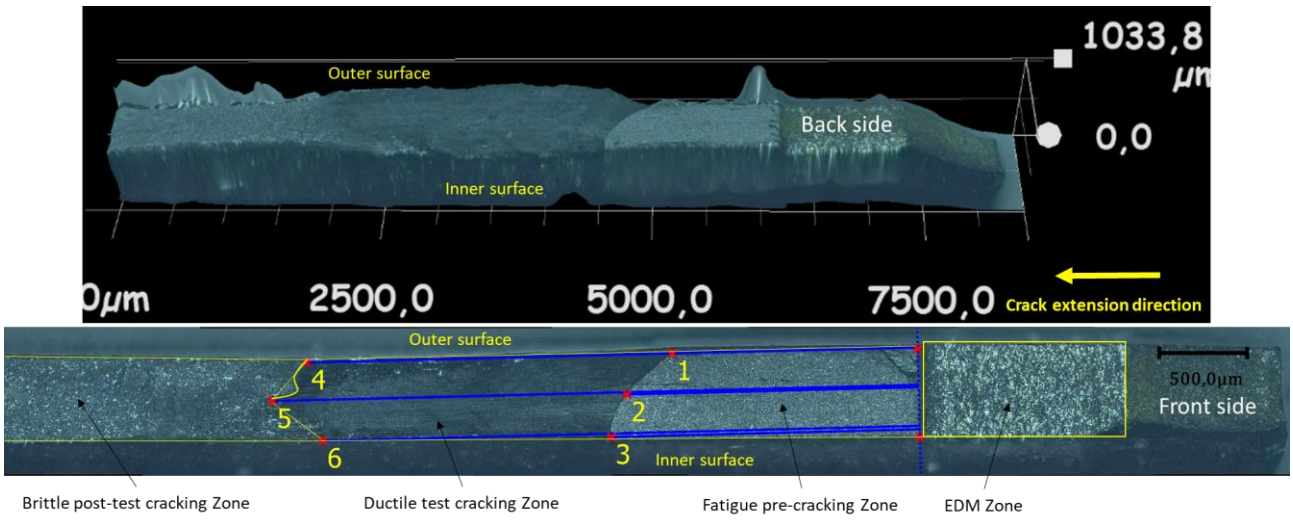

Fig. 4 Front and back sides failure surfaces with fatigue pre-crack and final crack extension measurement procedure

The fatigue pre-crack length and the final crack extension were then measured. After testing, the crack front of the PLT specimen xas usually not straight (chevron shape in most cases, see points 4, 5, and 6 in Fig. 4). Crack lengths were measured by averaging the crack lengths on 3 points through the thickness, at the inner surface (weight: $1/4$), at the outer surface (weight: $1/4$), and at half-thickness (weight: $1/2$). The average of the front and back sides crack lengths was then considered as the final crack length of the specimen.

4. Determination of the geometric functions $a/W(u)$, $f(a/W)$, and $\eta_{pl}(a/W)$

This section is devoted to determining the functions needed to obtain $J - \Delta a$ curves from PLT tests. Several analytical and numerical methods are proposed in and their suitability to be used on PLT specimen is discussed.

4.1. Numerical procedures

Detailed finite element analyses of the PLT test were performed using Cast3M 21 [25], a multi-physics finite element code developed by CEA. Three functions needed to be determined. (i) The evolution of the compliance as a function of normalized crack length a/W. This function allowed estimating the crack extension during tests using the unloading compliance method. (ii) The function used to determine the stress intensity factor (and therefore the elastic part of the J integral): $f(a/W)$. (iii) The η_{pl} and γ_{pl} functions used to evaluate the plastic part of the J integral. All fits of the functions determined in this work were performed by polynomial regression with a coefficient of determination $R^2 \geq 0.99$. When needed, the order of the function was increased to obtain this value. All the methods presented in sections 4.2, 4.3 and 4.4 have been tested by FEA on a standard C(T) specimen in the range of a/W recommended by the ASTM E1820-22e1 standard. The determined geometric functions cited in (i), (ii) and (iii) were in accordance with the corresponding ones given by ASTM E1820-22e1 standard [1].

The finite elements (FE) mesh with the boundary and loading conditions is presented in Fig. 5-a. Due to symmetries, a quarter of the assembly was modelized using linear quasi-incompressible hexahedral elements. While the mesh was quite refined, this element type gived the same results as quadratic hexahedral elements with reduced computation time. A finite strain framework was employed based on the Jauman stress rate. The mesh was refined around the crack tip to obtain a converged macroscopic load and a detailed description of the stress field in this area. The specimen loading was imposed by the displacement of the pin axis. Contact with a friction coefficient of 0.3 was used between the internal surface of the specimen and the mandrel to describe the experimental setup realistically. This friction coefficient was determined by performing tribological tests. A radial gap of 0.065 mm was also introduced between the mandrel and the inner surface of the specimen in agreement with the design of the setup (Fig. 5-b). This gap has an important effect on the mechanical response of the setup and may, in part, be responsible for some scattering of test results.

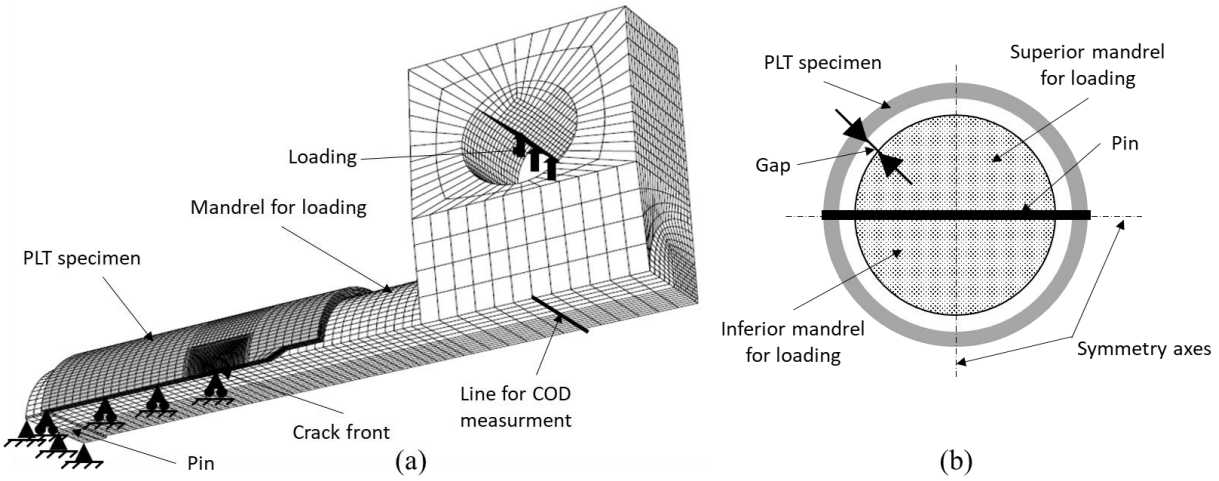

Fig. 5 (a) Finite element model with boundary conditions of the test setup (b) Sketch of left view of PLT assembly

The hardening behavior of the material was identified using ring tensile tests. This type of tensile test is often used to characterize the circumferential tensile properties of fuel cladding [2], [9], [26]. Based on the almost isotropic microstructure observed on the EBSD maps, the mechanical properties of the 9Cr ODS steel fuel cladding were supposed to be isotropic. Tile tensile tests were realized, as done before by Jaumier *et al*. [27]. These tensile tests allowed to verify and confirme that the use of Von Mises stress was available for our material. The flow stress was represented by the following function, which includes two Voce-type laws:

$$\sigma = 910 + 89.7(1 - e^{-492.9\,\varepsilon_p}) + 180.2(1 - e^{-28.3\,\varepsilon_p}) \quad \text{(MPa)} \tag{7}$$

Where σ is the stress and ε_p the cumulated plastic strain. The Young's modulus equals 225 GPa for the tested material and 214 GPa for the mandrel. The Poisson's ratio was set to 0.3. For elasto-plastic calculations, plastic flow is assumed to follow von Mises plasticity criterion

4.2. Determination of $a/W(u)$ function

The elastic unloading compliance method consists of measuring the compliance from elastic unloads applied during the test. From the measured compliance, a/W is determined using the normalized crack length function $a/W(u)$ given by the ASTM E1820-22e1 standard for standard specimens [1]. $a/W(u)$ is specific to the specimen geometry and had to be determined for the PLT specimens. To determine this function FE calculations of PLT test were performed for different crack lengths. In this case, the material was considered elastic, and small strains/small displacements were assumed.

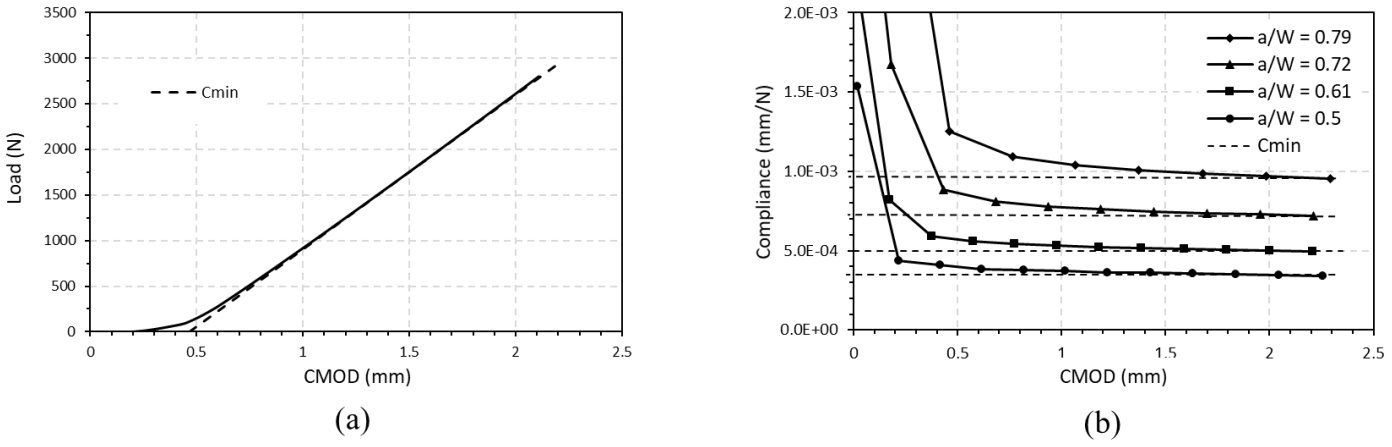

Fig. 6 (a) Elastic Load-CMOD curve for a given $a/W = 0.61$. (b) Compliance-CMOD curve showing the determination of C_{min}

Because of progressive contact, the Load-CMOD curve is not linear for low load levels, as exemplified in (Fig. ***6***-a). It is also possible to mimic the experimental procedure by performing partial unloadings during the simulation to compute

the unloading compliance. It is shown that it decreases as the CMOD increases and reaches a stable value (C_{min}) while contact between mandrel and internal surface of the specimen is fully established around the crack tip, provided the CMOD is large enough, as shown in Fig. 6-b for different values for a/W. This value is used to determine the $a/W(u)$ function.Several FE analyses of the PLT test in a normalized crack length range of $0.47 \leq a/W \leq 0.82$ were carried out. a/W is plotted a function of the normalized compliance $u = C \times E \times B$ (where B is two times the wall thickness t). The $a/W(u)$ function is fitted by a second-order polynomial equation as:

$$a/W(u) = -8.9441\ 10^{-6}\ u^2\ +\ 4.741\ 10^{-3}\ u\ +\ 2.0084\ 10^{-1} \tag{8}$$

Whatever the material, this function allows determining crack extension during the test for the present PLT specimen by subtracting the initial crack length a_0 from the instantaneous crack length at unload (i) a_i.

Rotation correction: The evaluations of the compliance and the $a/W(u)$ function are performed assuming small strains and do not reflect changes in specimen geometry due to large rotations as the test progresses. For that reason, the measured compliance must be corrected to be able to apply equation (8). The PLT specimen is loaded similarly to C(T) specimen (pin-loaded specimen in bending). It is therefore proposed to use the rotation correction proposed in the ASTM E1820-22e1 standard [1] for the C(T) specimen in the case of the PLT test. However, the material of this study does not exhibit a high toughness, so the rotation correction hardly affects the results.

4.3.Determination of $f(a/W)$

According to equations (2) and (3), the geometric function $f(a/W)$ is needed to evaluate the stress intensity factor K_I and deduce J_{el} . In case of the PLT specimen, Grigoriev et al. [5], Sanyal and Samal [28], Alvares Holston et al. [29], and Nitu et al. [10] proposed geometry-dependent functions for their PLT specimens. The $f(a/W)$ functions proposed by these authors are applicable to their specific specimen geometry. In this study, a suitable geometric function was evaluated for the used specimen geometry. Simulations already performed to evaluate the compliance (section 4.2) can be used for that purpose. $f(a/W)$ is evaluated for the linear part of the Load-CMOD curve. To calculate the geometric function, Grigoriev et al. [5] used a method based on compliance and hereafter referred to as the "Compliance method". A second method, used, *e.g.*, by Cravero and Ruggieri [30], is based on the direct evaluation of the J integral. It will be referred to as the "G_θ method“ [31]. In this section, both methods are applied and compared.

4.3.1. Compliance method

This method consists in determining the evolution of the compliance as a function of a/W and deducing the geometric function from $C(a/W)$ using the following equation:

$$f(\mathrm{a}/W) = \sqrt{\frac{BE}{2}\frac{\partial C}{\partial\left(\frac{a}{W}\right)}} \tag{9}$$

The compliance ($C_{\min}$ in the present case, as shown in Fig. 6-b,) is first fitted and is given as follows:

$$C(a/W) = \frac{1}{EB}\left[18\ 234.5\ \left(\frac{a}{W}\right)^4 - 43\ 784.1\ \left(\frac{a}{W}\right)^3 + 39\ 739.5\left(\frac{a}{W}\right)^2 - 15\ 779.6\frac{a}{W} - 2\ 360.5\right] \tag{10}$$

for values of a/W between 0.47 and 0.82. The fitted function is shown in Fig. 7. The geometric function $f_K(a/W)$ is then given following equation (11) as:

$$f(\mathrm{a}/W) = \sqrt{\left(\frac{1}{2}\left(72\ 938.1\ \left(\frac{a}{W}\right)^3 - 131\ 352.3\left(\frac{a}{W}\right)^2 + 79\ 479.1\left(\frac{a}{W}\right) - 15\ 779.6\right)\right)} \tag{11}$$

It is plotted in Fig. 9.

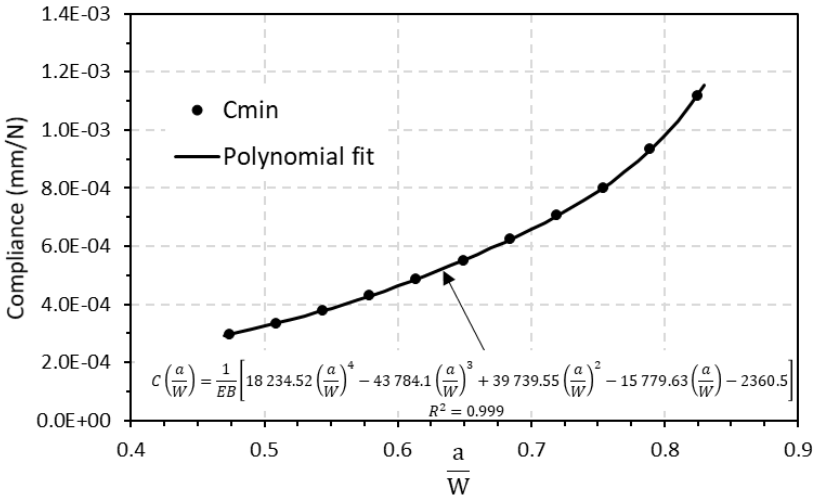

Fig. 7 C_{min} as function of a/W plot and polynomial fit of $C(a/W)$

4.3.2. G_θ method

This method consists in calculating the J-integral using a domain integral (G_θ method) implemented in Cast3M 21 [25]. The chosen integration domain has little influence on the computed J values as the simulation assumes elastic behavior. From the evaluation of J, K_I can be directly determined using equation (2). K_I is plotted as a function of $P/B\sqrt{W}$ in Fig. 8. The relation between both quantities is not linear for first load levels due to the progressive formation of the contact area between the specimen and the mandrel (see appendix). The linear part of the curve is used to determine $f_K$for the considered crack length. Note that contact formation appears to have less effect on the linear relation between K_I and $P/B\sqrt{W}$ than between Load and CMOD (see Fig. 6-a). Values for $f(a/W)$ for the different analyzed crack lengths are then plotted (see Fig. 9) and fitted by 3th order polynomial equation as:

$$f(a/W) = 709.76\left(\frac{a}{W}\right)^3 - 1277.06\left(\frac{a}{W}\right)^2 + 792.90\left(\frac{a}{W}\right) - 155.12 \quad (12)$$

with a coefficient of determination such that $R^2 \geq 0.99$.

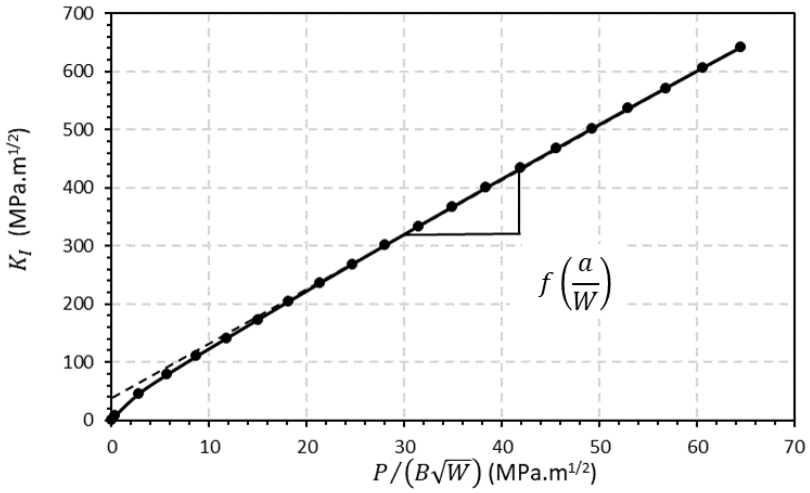

Fig. 8 Geometric function determination for $a/W = 0.47$

4.3.3. Comparison of the $f(a/W)$ functions and discussion

Values of f as a function of a/W for CEA PLT specimen geometry are plotted in Fig. 9 and compared with those obtained in the literature for different geometries of PLT specimens (the dimensions are recalled in the table in Fig. 9). The comparison of the values for the geometry of this study obtained with both methods (compliance and G_θ) is also given Fig. 9. Some small differences exists and it is believed that the "G_θ method" provides more reliable results as the

values for f are directly obtained from the FEA whereas the "compliance method" uses the derivative of a fitted function. This is known to lead to systematic errors [32].

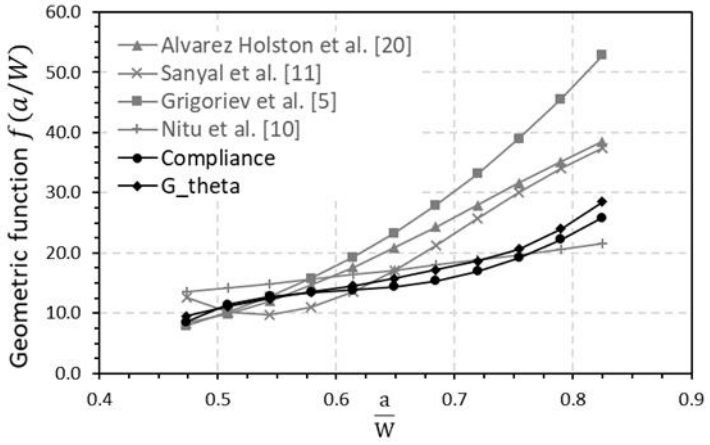

PLT Specimen	Wall thickness t (mm)	External diameter D (mm)	Tube length L (mm)
CEA (this study)	0.5	10.73	17
Alvarez Holston et al. [20]	0.57	9.5	13
Sanyal et al. [11]	0.9	14.2	13
Grigoriev et al. [5]	0.57	/	13
Nitu et al. [10]	0.6	10.9	10

Fig. 9 Comparison of geometric functions determined by compliance method and G_θ method to those proposed in the literature (PLT specimens dimensions are referenced in the table at the right)

4.4. Determination of η_{pl}

As presented in section 2, the plastic factor η_{pl}, and the correction factor γ_{pl} in case of a propagating crack, are needed to calculate J_{pl}. These factors are geometry dependent and have to be determined for nonstandard specimens. Some methods allowing the determination of these factors were proposed in the literature. Sharobeam and Landes [33], [34] proposed a method using the load separation theory of Ernst et al. [35] to determine η_{pl} when the plastic deformation in confined to the remaining ligament, which is the case for PLT specimens in 9Cr ODS steel. This method is referred to as the "S_{ij} method". Based on the same theory Sanyal et al. [11] used the "limit load" method" to determine η_{pl} and γ_{pl} and determine $J-$R curve of a Zircaloy fuel cladding using the PLT test [14]. Previously, Grigoriev et al. [36] had determined the $J-$R curve for the same material using the PLT, but they used the η_{pl} and γ_{pl} functions for C(T) specimens. A third method, consists of directly computing J from a domain integral (G_θ method in this work) to determine η_{pl}. This method is, e.g., used by Cravero and Ruggieri [30]. Once η_{pl} is determined, γ_{pl} can be deduced using equation (6). To determine η_{pl} (whatever the method), the mesh and boundary conditions shown in Fig. 5-a are still used. A finite strain framework accounts for plasticity (flow stress given by equation (7). In all cases,η_{pl} is determined for a/W between 0.47 and 0.82.

4.4.1. S_{ij} method

This method was proposed by Sharobeam and Landes [33], [34] and was validated on several materials for different standard fracture mechanic specimens geometries. It is based on the load separability theory of Ernst et al. [35], [37] that stipulate that the η_{pl} factor only exists if P can be represented in a separable form as follow:

$$P\left(\frac{b}{W};\frac{V_{pl}}{W}\right) = G\left(\frac{b}{W}\right) \times H\left(\frac{V_{pl}}{W}\right) \tag{13}$$

Where b is the ligament size ($b = W - a$), and V_{pl} the irreversible (plastic) CMOD. G and H are two functions that are *a priori* unknown. They then introduced a separation parameter S_{ij}. This parameter is the ratio between loads for specimens with different crack lengths at the same plastic displacement. In the case of a non-propagating crack, for two specimens with uncracked ligament lengths b_i and b_j, S_{ij} is constant whatever the plastic displacement and can be written referring to equation (13) as

$$S_{ij} = \frac{P\left(\frac{b_i}{W}, \frac{V_{pl}}{W}\right)}{P\left(\frac{b_j}{W}, \frac{V_{pl}}{W}\right)} = \frac{G\left(\frac{b_i}{W}\right) H\left(\frac{V_{pl_1}}{W}\right)}{G\left(\frac{b_j}{W}\right) H\left(\frac{V_{pl_1}}{W}\right)} = \frac{G\left(\frac{b_i}{W}\right) H\left(\frac{V_{pl_2}}{W}\right)}{G\left(\frac{b_j}{W}\right) H\left(\frac{V_{pl_2}}{W}\right)} = \frac{G\left(\frac{b_i}{W}\right)}{G\left(\frac{b_j}{W}\right)} \quad (14)$$

They demonstrated that, for a constant reference value for b_j/W, S_{ij} can be written as

$$S_{ij} = Constant \times \left(\frac{b_i}{W}\right)^{\eta_{pl}} = \left(\frac{b_i}{b_j}\right)^{\eta_{pl}} \quad (15)$$

The following procedure can then be applied to determine η_{pl}. (i) Select a reference uncracked ligament length b(j). (ii) Determine S_{ij} by plotting the ratio of the loads for two uncracked ligament lengths bi and bj as a function of V_{pl}. The curve should reach a constant value for sufficiently high values of V_{pl}.Note that, $S_{jj} = 1$. (iii) Plot the asymptotic separation parameter S_{ij} for different values of b_i/W and fit a power law function according to equation (15) to obtain η_{pl} which corresponds to the exponent of the power law. The procedure is applied in Fig. 10-a. S_{ij} varies until it converges to a constant value when the plastic displacement is larger than 1 mm. The fit of the power law leads to a η_{pl} parameter equal to 1.71 (Fig. 10-b). This method can be applied only to situations where η_{pl} is constant with a/W (i. e. SE(B) specimens), or has a weak dependence (C(T) specimens). In the case of PLT specimen, η_{pl} weakly depends on a/W in the range $0.5 \leq a/W \leq 0.7$ (see Fig. 13-a), hence S_{ij} method is applicable only in this range of a/W.

$\gamma_{pl} = \eta_{pl} - 1 = 0.71.$

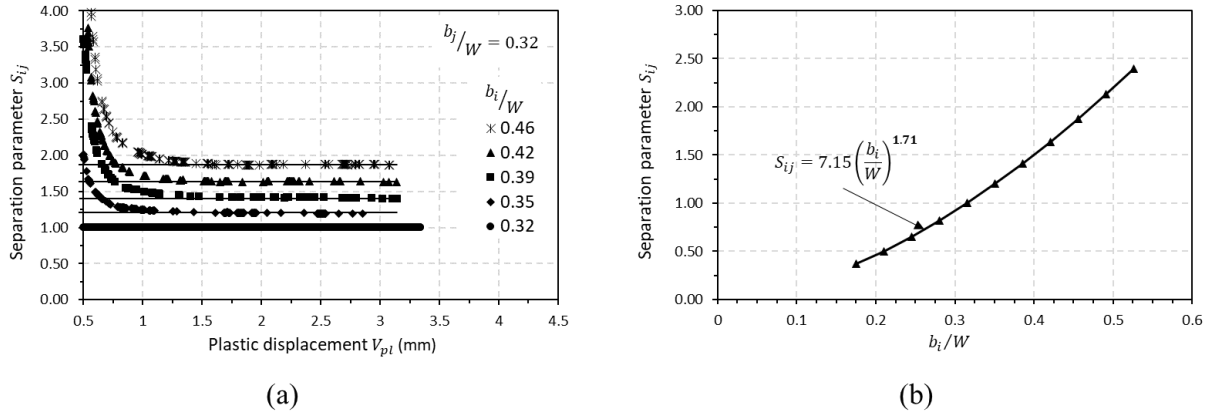

Fig. 10 (a) Separation parameters for a reference ligament length $b_j/W = 0.32$. (b) Power law fit of the separation parameter and determination of η_{pl}

4.4.2. Limit load (F_L) method

The limit load method has been validated on standard specimens by Anderson et al. [14]. Sanyal et al. [11] used this method to determine η_{pl} of their PLT specimens and to assess the fracture toughness of Zircaloy-4 fuel cladding. To apply this method, the expression of limit load F_L as a function of normalized crack length a/W is required. This function is assumed to be expressed using the following form:

$$F_L = \sigma_Y \, B \, W \, g\left(\frac{a}{W}\right) \quad (16)$$

where σ_Y is the flow stress corresponding to the average value between σ_{YS} (yield stress) and σ_u (ultimate tensile strength), and $g(a/W)$ a function dependent of a/W.

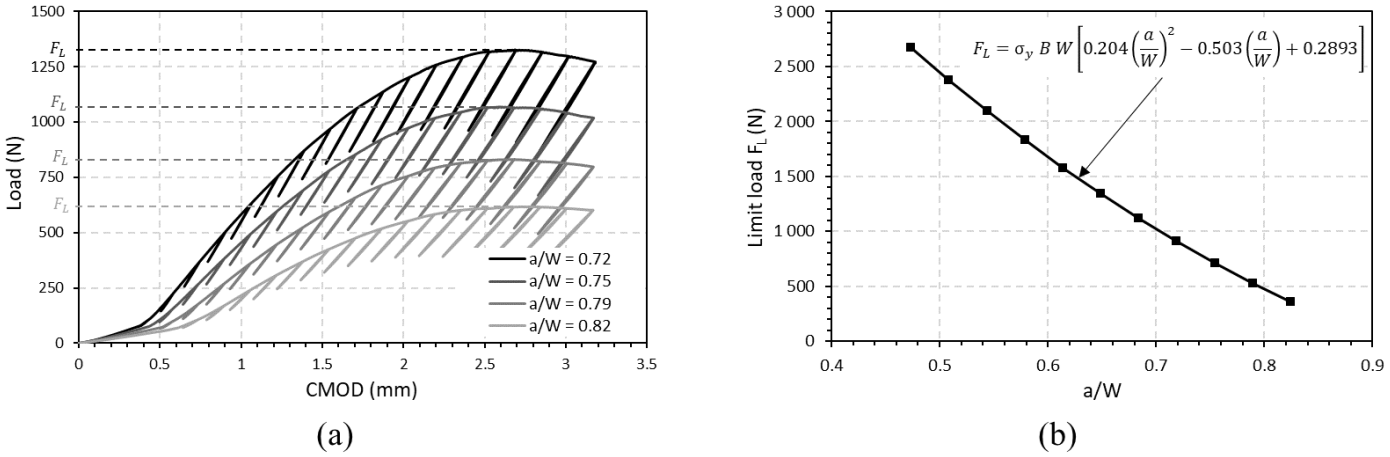

Fig. 11 (a) Limit load determination from FEA (b) 2nd order polynomial fit of Limit Load as a function of a/W

Then using $F_L(a/W)$ determined from elastoplastic FEA (see Fig. 11-a), the expression η_{pl} is determined from the following equation

$$\eta_{pl} = -\left(1 - \frac{a}{W}\right)\frac{1}{F_L}\frac{\partial F_L}{\partial\left(a/W\right)} \tag{17}$$

To apply this method, the limit loads obtained using finite element simulation of the PLT test for various crack lengths are plotted as a function of a/W. The resulting plot is shown in Fig. 11-b. This plot allows fitting the $g(a/W)$ function as a polynomial. η_{pl} is then expressed as follows, using equation (17)

$$\eta_{pl} = \left(1 - \frac{a}{W}\right)\frac{0.503 - 0.408\left(\frac{a}{W}\right)}{0.204\left(\frac{a}{W}\right)^2 - 0.503\left(\frac{a}{W}\right) + 0.2893} \tag{18}$$

4.4.3. G_θ method

This method is based on the calculation of the J-integral from a domain integral using the G_θ method already used above to determine $f_K(a/W)$. However, for an elastoplastic material as it is supposed here, the determined J-integral is the total J and has an elastic part and a plastic part b. By introducing the plasticity and large strains in the mechanical model, the J-integral determined by the G_θ method becomes more dependent on the integration domain than for the case of the elastic/small strains. The integration domain size was varied by taking different layers of elements. When taking a large enough domain for a given a/W, the value of the J-integral converges as shown in Fig. 12-a. The converged value of the J-integral is then taken into account in the analysis. J_{el} is calculated using the geometric function determined from the elastic FE analysis (FEA) (see section 4.3.2). J_{pl} is then calculated from equation (1). For a constant a/W, the evolution of J_{pl} as a function of the plastic area (A_{pl}) under the load-CMOD curve is supposed to be linear. As in the elastic case, the linearity of this curve is affected by progressive contact for the first loading steps. It becomes linear for higher levels and, being in static crack condition, its slope is η_{pl} multiplied by the constant value $1/Bb$ as shown in (Fig. 12-b).

The different values of η_{pl} determined for different a/W are then plotted and fitted (see G_theta plot in Fig. 13-a). The polynomial fit of the plot gives the following η_{pl} function

$$\eta_{pl} = 3.2674\left(\frac{a}{W}\right)^2 - 3.382\left(\frac{a}{W}\right) + 2.5622 \tag{19}$$

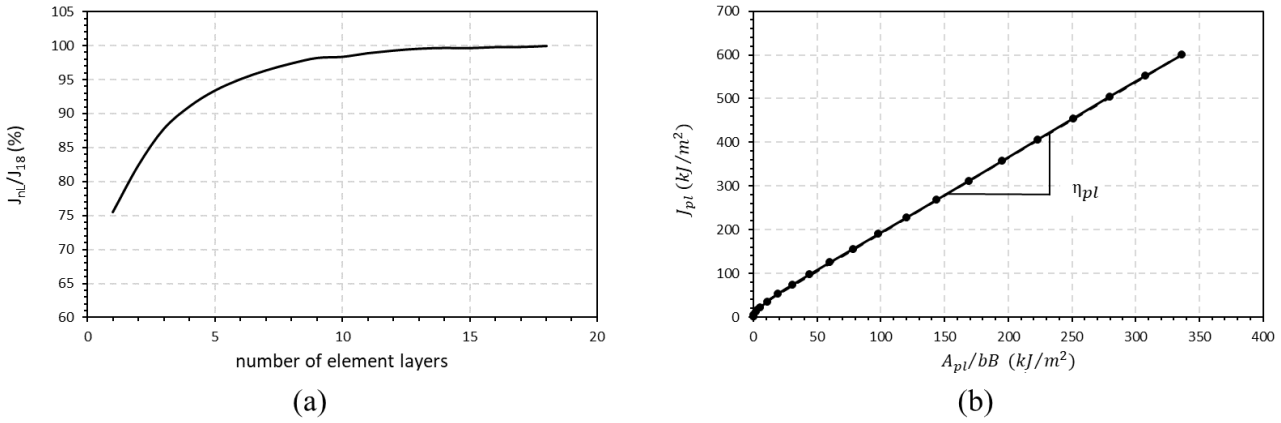

Fig. 12 (a) Relative J-integral as a function of the number of element layers (b) η_{pl} determination from the domain integral for $a/W = 0.61$.

4.4.4. Comparison of the plastic and correction factors and discussion

Three different methods have been applied to determine η_{pl} . The different fitted functions are plotted together with the results obtained by Sanyal et al. [11] for their specific PLT setup in Fig. 13-a. The results of Sanyal et al. [11] were checked using the "G_θ method" which gave similar results. The three methods give relatively equivalent η_{pl} values for the PLT specimen of this study. However the geometry used by Sanyal et al. [11] appears to be more sensitive to a/W. The S_{ij} method leads to a constant value for η_{pl}. It is therefore a suitable method in the case where η_{pl} is not very sensitive to a/W like for CEA ODS steels PLT specimens geometry. It can also be applied directly to experimental data (see Sharobeam and Landes [33], [34]) when the material is ductile enough. The limit load method is also a suitable method that can also be applied to experimental data to determine η_{pl} if the material is ductile enough so that the maximum load is reached before crack initiation. It also provides an η_{pl} factor that varies as a function of a/W but relies on the derivative of a fitted function. The "G_θ method" seems to be a more suitable method to determine η_{pl} for PLT specimens for the present material which exibits early cracking. It must be applied only using elastoplastic FE analysis of the test. In the case of the material of this study, which shows limited ductility, the two first methods cannot be experimentally applied to determine η_{pl}. However, the three methods are suitable when applied using FEA and give equivalent plastic factors as shown in Fig. 13-a.

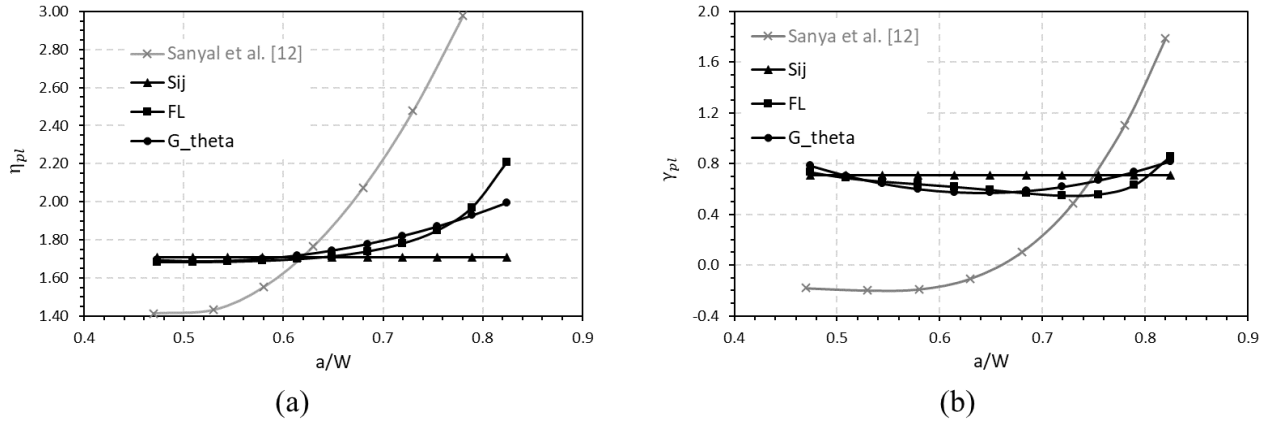

Fig. 13 (a) Comparison of the η_{pl} factors as a function of $/W$ (b) Comparison of the γ_{pl} factors as a function of a/W

The different γ_{pl} are calculated using the different η_{pl} functions using equation (6). As for η_{pl}, the three methods give equivalent γ_{pl} factors (see Fig. 13-b). The different determined η_{pl} and γ_{pl} give very similar $J-$R curves when applied to the experimental data.

4.5. Accounting for non-linearities due to contact between the specimen and the mandrels

As mentioned in section 4.3.2, K_I is not a linear function of $P/B\sqrt{W}$ at low loads due to the increase in the contact area between the specimen and the mandrels. In this previous section, f_K was evalulated considering the linear part of the curve corresponding to high values of K_I. As the ODS 9Cr steel shows a limited toughness, measured toughnesses (see

section 5) lie in the region where contact affects the values of f_K as the maximum value of K_J is 230 MPa$\sqrt{\text{m}}$. It can be observed in Fig. 14-a ($a/W = 0.47$) that the error in the estimation of K_I can be up to 33 MPa$\sqrt{\text{m}}$ which corresponds to the interpolated value of K_I at zero load (cross in Fig. 14-a). This value is about 30% of the maximum value of the "elastic" K_I reached during experimental tests. To quantify the effect of the initial fit, new values for f_K and η_{pl} are computed in the following by limiting the fit to low values of K_I. They are referred to as f_K^* and η_{pl}^*.

Determination of $f^*(a/W)$

f^* is computed for values of K_I between the origin and the point at which $K_I = 200$ MPa$\sqrt{\text{m}}$ which is the average maximum value of K_J obtained during the test using the original functions f_K and η_{pl}. A linear regression is used (dashed line in Fig. 14-a) with a determination coefficient equal to 0.988.The method is applied to different a/W in the range of 0.47 to 0.82 to determine the function $f_K^*(a/W)$ as follows:

$$f^*\left(\frac{a}{W}\right) = 434.383\left(\frac{a}{W}\right)^3 - 695.761\left(\frac{a}{W}\right)^2 + 414.764\left(\frac{a}{W}\right) - 75.243 \quad (20)$$

As shown in Fig. 14-b, $f_K^*(a/W)$ is larger than $f_K(a/W)$ as the initial slope is higher than the slope of the assymptote reached for high K_I (in Fig. 14-a).

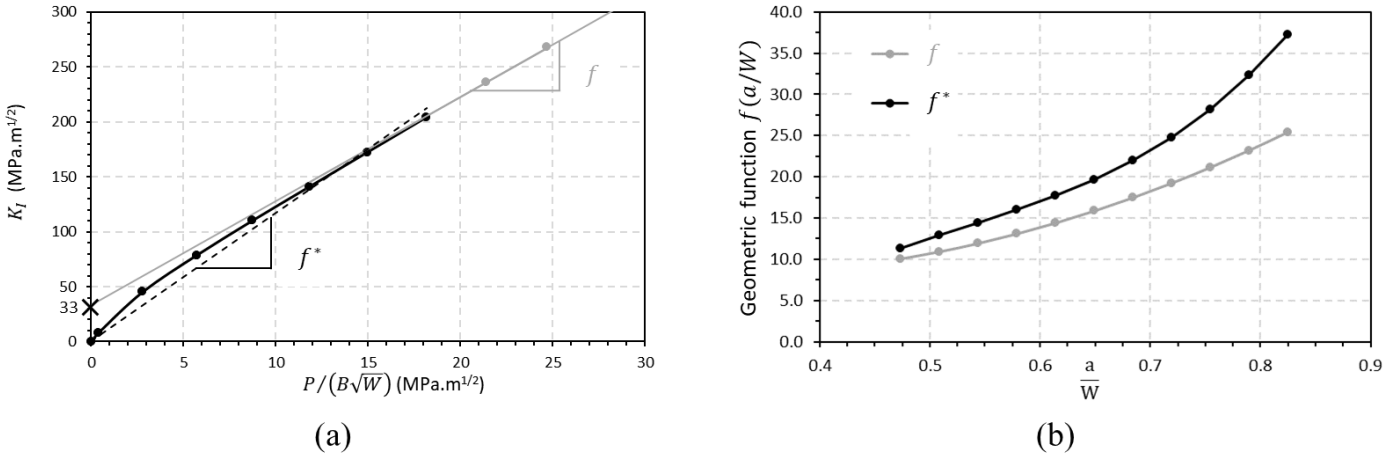

Fig. 14 (a) Determination of f^* for $a/W = 0.47$ (b) Comparison of $f(a/W)$ and $f^*(a/W)$

Determination of η_{pl}^*

To determine η_{pl}^*, the procedure explained in section 4.4.3. was again employed using the same values of the J integral. K_I and J_e were then determined determined for every a/W using $f^*(a/W)$ in equation (3)). This allows evaluating J_{pl} which is plotted against A_{pl}/Bb (see Fig. 15-a). It can also be observed from Fig. 15-a that the J_{pl}^* - A_{pl}/Bb curve shows a much smaller initial vertical offset than previously observed (see Fig. 12-b). This allows computing η_{pl}^* from the average slope of this curve. A linear regression is used (black line in Fig. 15-a) with a determination coefficient equal to 0.99. η_{pl}^* as a function a/W is fitted as shown by a polynomial function as (see Fig. 15-b):

$$\eta_{pl}^* = 6.8303\left(\frac{a}{W}\right)^2 - 8.1182\left(\frac{a}{W}\right) + 3.6764 \quad (21)$$

Fig. 15-b also shows that η_{pl}^* is smaller than η_{pl}. γ_{pl}^* can then be determined using equation (6) as for the other methods.

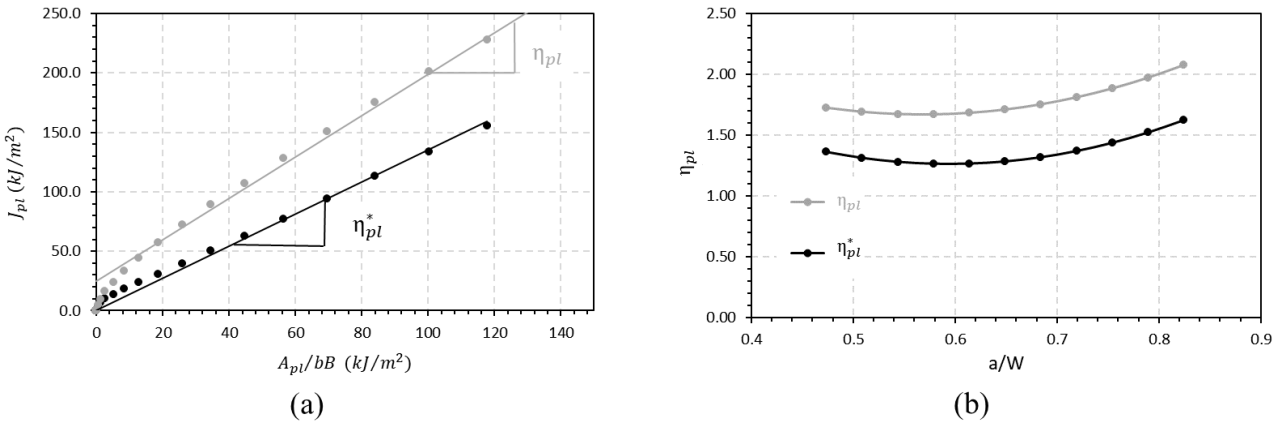

Fig. 15 (a) η^*_{pl} determination for $a/W = 0.47$ (b) Comparison of η^*_{pl} and η_{pl}

To evaluate if there is an effect on the determination of J-integral when using f^* and η^*_{pl} method rather than f_K and η_{pl}, the two methods have been applied to an experimental test. Fig. 16 shows that the $J-R$ curves obtained with both methods are equivalent but that the proportion between the elastic and plastic parts of the J-integral differ. When using f^*_K and η^*_{pl}, J_{el} is higher and J_{pl} is consequently lower. It can be concluded that the use of either method affects the values of J_{el} and J_{pl} without affecting the total value of the total J-integral. When using f^* and η^*_{pl}, the non-linearity at early stages of the PLT test are taken into account, which makes these two functions more adapted to materials that show early cracking as for the material of the study.

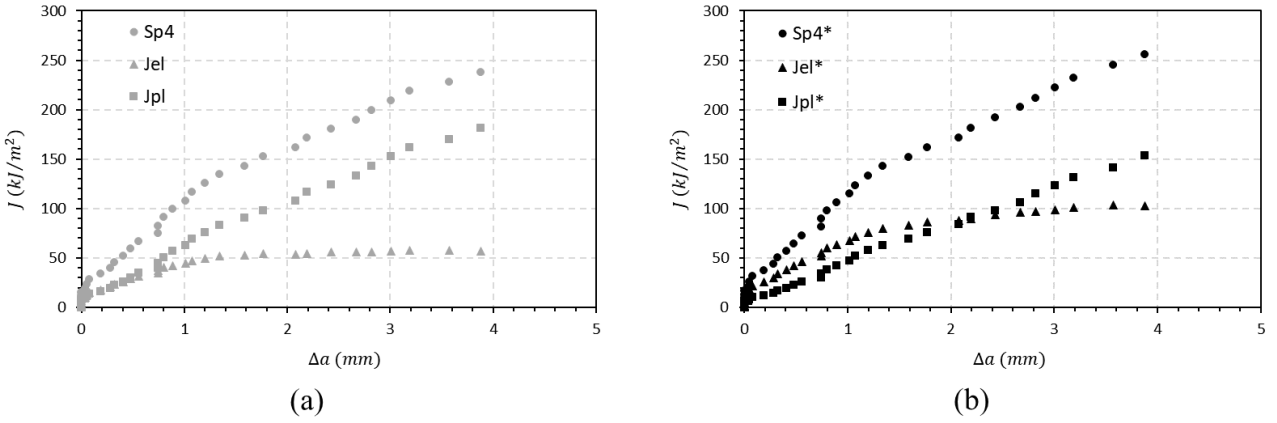

Fig. 16 (a) J, J_{el} and J_{pl} as functions of Δa determined using f_K and η_{pl}. (b) J, J_{el} and J_{pl} as functions of Δa determined using f^* and η^*_{pl} (Sp4 test).

Note: The determination of f^* and η^*_{pl} depends on the value of K_I selected for the linear fit of f^* (200 MPa√m in this work). However, if a different value is chosen, the values of J_e et J_p will be changed but $J = J_e + J_p$ will also remain unchanged. Another solution would be to express f^* and η^*_{pl} as functions of a/W and the load P. This solution is believed to be too complex for practical applications.

5. Experimental results and discussion

Experimental PLT tests were carried out on the CEA 9Cr ODS steel fuel cladding material under the conditions discussed in section 3.2. Several specimens with different a_0 were tested as presented in Table 2. From the optical tracking of crack extension, it was noticed that crack initiation occurs before the opening displacement reaches $\mathrm{CMOD}_{C_{\min}}$, *i.e.*, the crack opening displacement corresponding to $C_{\min}$. Hence, when $\mathrm{CMOD} \leq \mathrm{CMOD}_{C_{\min}}$ recorded images were used to determine crack propagation Δa (Fig. 17). Crack advance at $C_{\min}$ is between 400 and 700 μm depending on the specimen. Beyond that point, the unloading compliance method is applied to determine crack extension using equation (8). Final crack extensions Δa_f were measured on fracture surfaces following the procedure discussed in section 3.3. To validate the application of the unloading compliance method, the estimated final crack propagations Δa_f are compared to those measured *post-mortem* following the procedure discussed in section 3.3. As presented in Fig.

18, the unloading compliance estimated Δa_f are in accordance with those measured post-mortem with an average error of 7.7%. From recorded images, a crack deviation is observed at the beginning of the test. The crack deviates from the middle plane before it progresses following the propagation axis (the longitudinal direction) after a crack extension of about 400 µm (see Fig. 17-(d)). This is due to a rotation of about 45° of the crack plane. This deviation is often observed for cracks propagating in sheets (see, *e.g.*, Besson et al. [38] and El Naaman et al. [39]). It may be facilitated by the through-thickness stress heterogeneity in the crack front region, as shown in the appendix (see A.1).

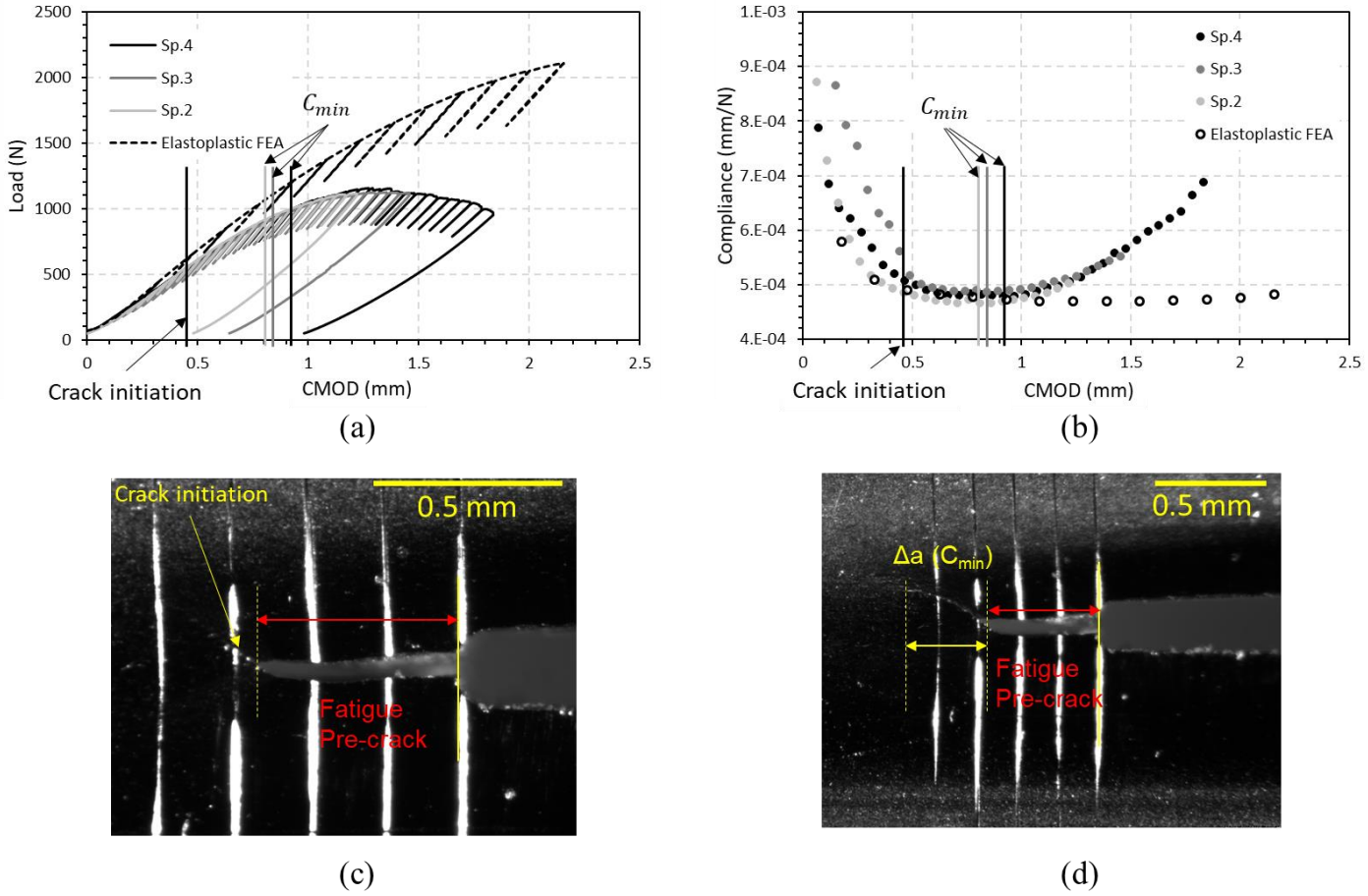

Fig. 17 (a) Experimental and simulated Load-CMOD curves. (b) Experimental and simulated compliance-CMOD curves. (c) Crack opening at crack initiation. (d) Crack opening and advance at C_{min}.

The tests were simulated using the FE method, including the partial unloading to mimic the experiments (Fig. 17-a). It is shown that the decrease in compliance with increasing CMOD is well described (Fig. 17-b). As the FE model does not include the simulation of cracking, the increase in compliance after crack initiation is indeed not reproduced. $f(a/W)$, η_{pl} and γ_{pl} determined by the G_θ method were used to analyze the PLT tests and obtain the resistance curves. Experimental $J-$R curves are plotted in Fig. 19-a. A relatively small scatter is obtained. Scatter is attributed to variations in the gap existing between the specimen and the mandrels, as shown in the appendix. A power law fit of each $J-$R curve is then performed as $J = C\,\Delta\, a^m$ as recommended in the ASTM E1820-22e1 standard [1]. The blunting line that corresponds to $J = 2\sigma_y \Delta a$ and parallel lines with an offset of 0.2 mm and 1 mm are drawn. The intersections of the fitted $J-$R curve with both lines are used to evaluate $J_{0.2}$ and J_1(Fig. 19-b). Mean values of $J_{0.2} = 34.7 \pm 6.6$ kJ/m^2 and $J_1 = 102.4 \pm 7.5$ kJ/m^2 are then determined. The use of a slope of $2\sigma_y$ for the blunting line is proposed by ASTM E1820-22e1 [1] for standard test and can be discussed. It has been used in this study so that the obtained results are comparable with the previous ones on other materials using PLT test [11]. The use of an unlimited slope would be suitable regarding to the direct method used to determine the crack length at the first stages of crack extension.

According to ASTM E1820-22e1 standard [1], $J_{0.2}$ can be considered as a fracture toughness value J_{IC} if the initial uncracked ligament b_0 and the specimen thickness B verify the following condition:

$$B, b_0 > 10\,J_{0.2}/\sigma_Y \tag{22}$$

This means that the intersection between the power law fit and the 0.2 mm offset line falls in the ASTM E1820-22e1 box that indicates valididity limits delimited by J_{max} and Δa_{max} dashed lines. Considering that B corresponds to two times the wall thickness (t). Because the fracture surface is composed of two independent surfaces, it is better to check that the above condition is valid considering t instead of B. The corresponding $K_{J_{0.2}}$, is considered the critical stress intensity factor at crack initiation, and is determined in plane stress condition as

$$K_{J_{0.2}} = \sqrt{J_{0.2}E} \tag{23}$$

A value of 88.3 ± 8.2 MPa.m$^{1/2}$ is obtained. Following ASTM E1820-22e1 standard [1], the 9Cr ODS steel PLT specimens verify the condition given by equation (22) as one gets $(10J_{0.2})/\sigma_Y = 350\mu\text{m} < \text{t} = 500\mu\text{m}$. $K_{J_{0.2}}$can be considered as $K_{J_{IC}}$.

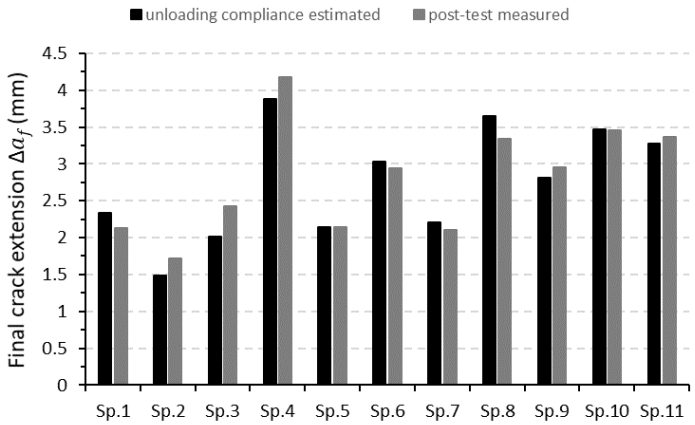

Fig. 18 Comparison between crack extensions determined from unloading compliance estimates and *post-mortem* measurements.

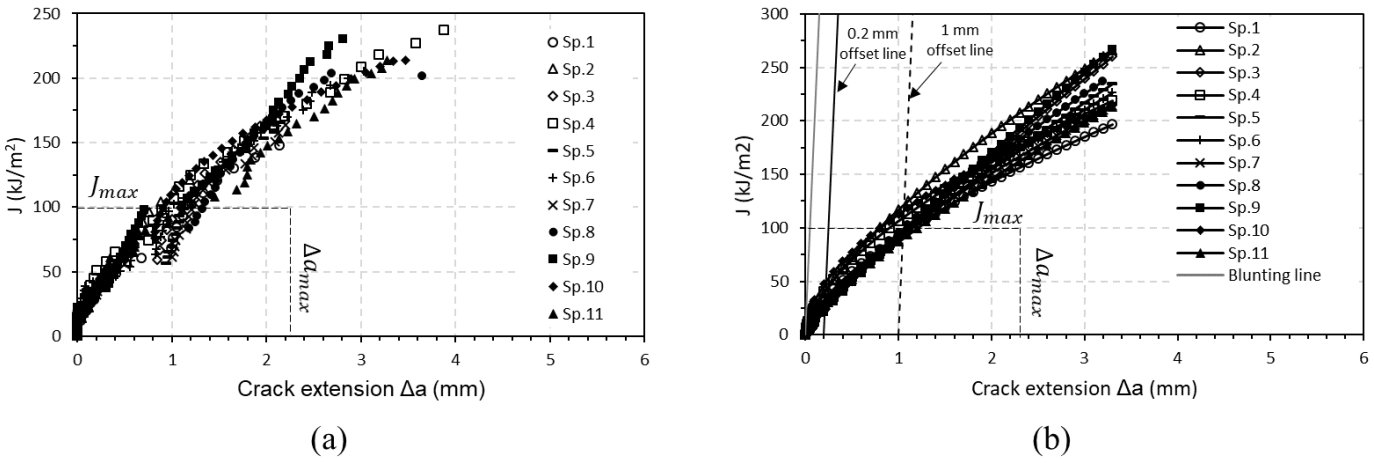

Fig. 19 (a) Experimental $J-R$ curves obtained using the developed method. (b) Power law fits of the $J-R$ curves and determination of $J_{0.2}$ and J_1

6. Conclusion

In this paper, the PLT test was used to determine the fracture toughness of 9Cr ODS steel fuel cladding. A single specimen method based on the use of the unloading compliance method was developed and used because the material is scarce, especially when irradiated. Detailed FEA of the PLT test set was conducted to simulate the pre-cracked specimen behaviour during testing. This simulation was used to determine the geometric functions $f(a/W)$, $a/W(u)$, η_{pl} and γ_{pl} needed to run and analyze the test following the procedure proposed by ASTM E1820-22e1. It was shown that progressive contact between the specimen and the mandrels affects the results. In addition, it was observed (see

appendix) that bending exists along the crack front. This phenomenon is related to the design of the PLT test but has not previously been addressed in the literature. However, the developed procedure allows for determining the $J-\mathrm{R}$ curve.

Several tests were carried out and a good reproducibility of the obtained $J-\mathrm{R}$ curves is observed. The low scatter is mainly attributed to the variation of the gap between the internal radius of the PLT specimen and the radius of the mandrels. It is recommended to minimize the gap to limit the progressive contact. The limited ductility of the material implied the use of a direct method to determine the crack extension at the beginning of the test to have a better determination of the fracture tiughness at initiation. In the case of more ductile materials, the developed method is likely to be directly applicable without relying on optical measurements of crack extension.

Despite its main drawback (contact with the mandrels), the method shows potential to run PLT tests on irradiated cladding materials in hot cells. Indeed this type of characterization is required for the integrity assessment of all the type of fuel claddings used in nuclear reactors. Further developments of the test method will include testing at high temperatures to be more representative of in-service conditions.

Acknowledgements

The authors would like to thank D. Sornin (CEA/DES/ISAS/DRMP/SRMA/LTMEX) and the LTMEX laboratory from the CEA for the manufacture of the ODS steel fuel claddings studyed in this paper.

They also would like to thank E. Rouesne (CEA/DES/ISAS/DRMP/SRMA/LA2M) for the production of the EBSD maps

Appendix: Study of bending through the thickness and effect of the gap

It is experimentally and computationally observed that the Load-CMOD curve during a PLT test is not linear at the beginning of the test. This behavior is related to the change in the contact surface between the specimen and the mandrel. To better understand the loading of the specimen, the contact surface and stress profiles along the crack propagation were investigated. Opening stress profiles are taken at the outer surface, the inner surface, and the center of the specimen. Three loading steps are considered (witout taking into account crack advance): (a) crack initiation as observed during the test (*i.e.*, $\mathrm{CMOD} \approx 0.5\mathrm{mm}$), (b) when $C_{\min}$ is reached (*i.e.*, $\mathrm{CMOD} \approx 1\mathrm{mm}$), (c) at a load point for which the specimen undergoes large-scale yielding ($\mathrm{CMOD} \approx 1.8\mathrm{mm}$). Results are shown in A.1.

The contact surface increases with increasing load. At low load, the stress profiles show bending close to the crack tip, with the inner surface being in tension and the outer surface in compression. This is due to an unfolding of the side edges of the specimen until it matches the shape of the mandrels close to the crack tip. As load increases, this effect is suppressed at the crack tip. Opening stresses are close to 0 at the center of the ligament. On the rear side of the specimen, bending is always observed, with the inner surface being in compression and the outer surface in tension. At this location, bending appears to increase with increasing load. These results indicate that even though the specimen may geometrically resemble a C(T) specimen, its mechanical state strongly differs.

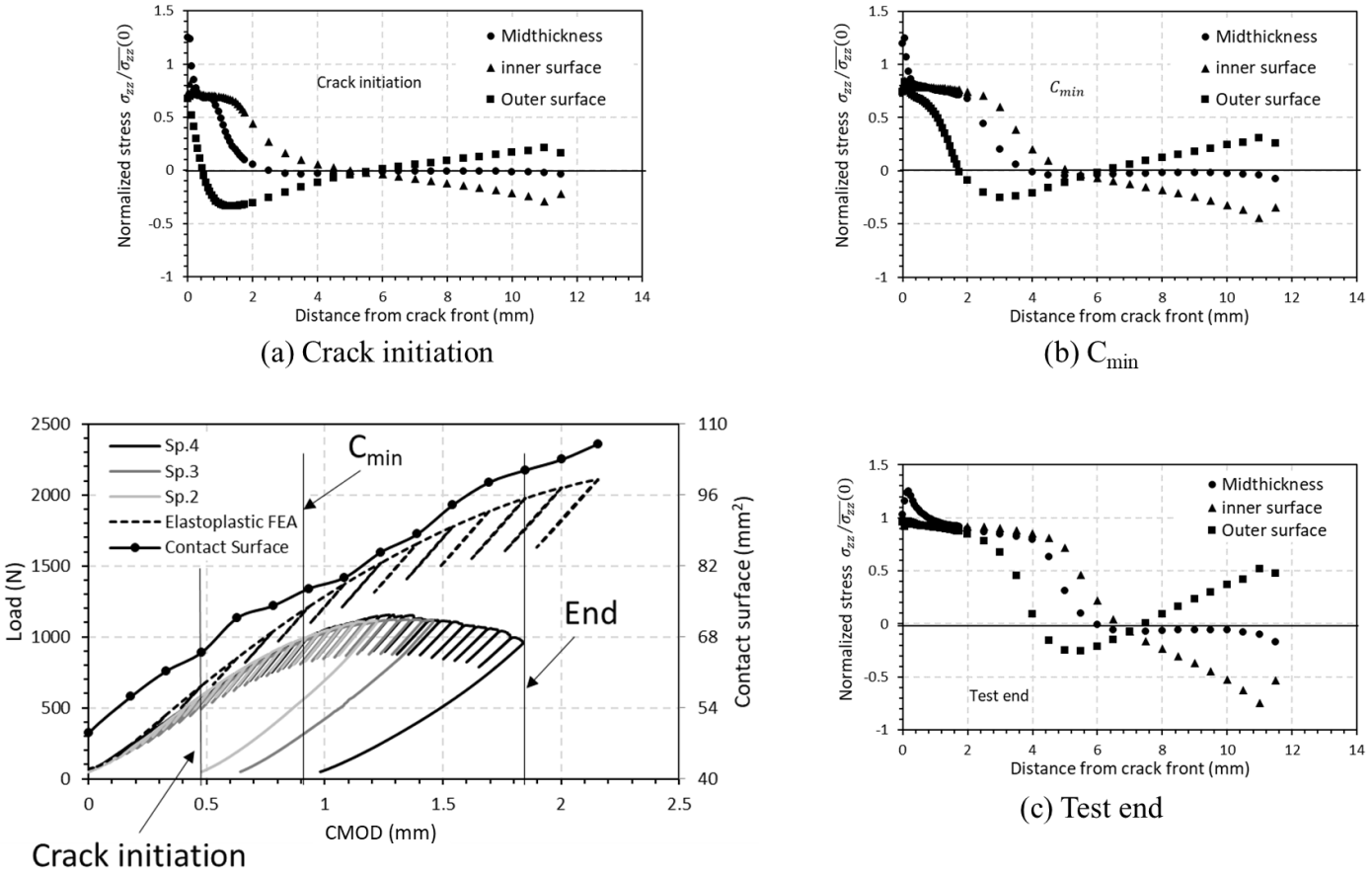

A.1 Evolution of contact surface with uncracked ligament stress profiles at (a) crack initiation (b) C_{min} (c) end

The effect of the gap between the specimen and the mandrel was also studied. The specimen's compliance was evaluated as a function of a/W for values of the gap equal to 10, 65 (nominal value), and 100 μm. Results are shown in A.2. It is shown that most of the experimentally determined values lie between the bound obtained using the minimum and maximum values for the gap. It can be concluded that the scatter observed for the determination of crack extension is mainly due to the variations of the tube diameter due to manufacturing.

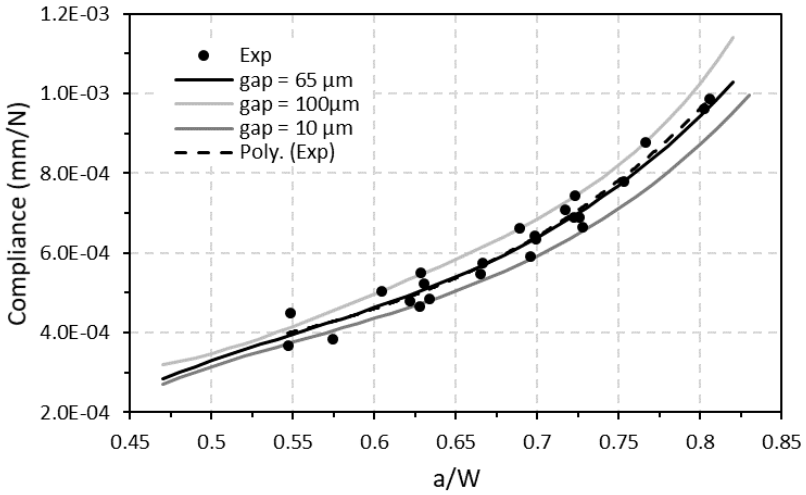

A.2 (a) Compliance as a function of normalized crack length for various gaps and comparison with experiments.

References

[1] American Society for Testing and Materials. Standard Test Method for Measurement of Fracture Toughness. ASTM E1820-22e1; 2022., .

[2] T. Jaumier, S. Vincent, L. Vincent, S. Desmorat. Creep and damage anisotropies of 9%Cr and 14%Cr ODS steel cladding. Journal of Nuclear Materials 2019; 518:274-286., .

[3] H. Salmon-Legagneur, S. Vincent, J. Garnier, A. F. Gourgues-Lorenzon, E. Andrieu. Anisotropic intergranular damage development and fracture in a 14Cr ferritic ODS steel under high-temperature tension and creep. Materials Science and Engineering: A 2018; 722:231-241., .
[4] L. Toualbi, C. Cayron, P. Olier, J. Malaplate, M.-H. Mathon, E. Rouesne et al. Assessment of a new fabrication route for Fe–9Cr–1W ODS cladding tubes. Journal of Nuclear Materials 2012; 428:47-53., .
[5] V. Grigoriev,B. Josefsson, A. Lind. A pin-loading tension test for evaluation of thin-walled tubular materials. Scripta Metallurgica et Materialia 1995; 33:109-114., .
[6] HH Hsu, KF Chien, HC Chu, PK Liaw. An X-Specimen Test for Determination of Thin-Walled Tube Fracture Toughness. ASTM STP 1406, R. Chona, Editors. Fatigue and Fracture Mechanics, West Conshohocken, PA: American Society For Testing and Materials; 2001, p. 214-226.,
[7] C Sainte-Catherine, D Le Boulch, S Carassou, C Lemaignan. An Internal Conical Mandrel Technique for Fracture Toughness Measurements on Nuclear Fuel Cladding. Journal of Testing and Evaluation 2006; 34:373-382., .
[8] A. Likeb, N. Gubeljak, Y. G. Matvienko. Finite element estimation of the plastic η_{pl} factors for pipe-ring notched bend specimen using the load separation method. Fatigue & Fracture of Engineering Materials & Structures 2014; 37:1319-1329., .
[9] P. Yvon, C. S. Catherine, C. Duguay, N. Hourdequin, S. Carassou, B. Cazalis, C. Bernaudat. Development of new techniques to assess the mechanical behaviour of Zircaloy-4 during an RIA. Fuel behaviour under transient and LOCA conditions 2002; 111-122, .
[10] A. Nitu, M. Abrudeanu, V. Radu. New Fracture Mechanics Method for the ODS Steel Testing. Journal of Nuclear Research and Development 2018; 21-28., .
[11] G. Sanyal, M.K. Samal, J.K. Chakravartty, A.K. Suri. Prediction of J–R curves of thin-walled fuel pin specimens in a PLT setup. Engineering Fracture Mechanics 2011; 78:1029-1043., .
[12] HA Ernst, P. C. Paris, J. D. Landes. Estimation on J-Integral and Tearing Modulus T from a Single Specimen Test Record. Fracture Mechanics:Thirteenth Conference. ASTM STP 743, Richard Roberts, Editors. American Society for Testing and Materials; 1981, p. 476-502., .
[13] J. R. Rice, P. C. Paris, J. G. Merkle. Some Further Results of J-Integral Analysis and Estimates. ASTM International, J. G. Kaufman, J. L. Swedlow, H. T. Corten, J. E. Srawley, R. H. Heyer, E. T. Wessel, G. R. Irwin, Editors. Progress in Flaw Growth and Fracture Toughness Testing, 100 Barr Harbor Drive, PO Box C700, West Conshohocken, PA 19428-2959; 1973, p. 231-245.,
[14] T.L. Anderson. Fracture Mechanics: Fundamentals and Applications. 3rd ed. 6000 Broken Sound Parkway Northwest, Boca Raton; 2017.,
[15] L. Toualbi, Optimisation de la gamme de fabrication de tubes en aciers renforcés par une dispersion nanométrique d'oxydes (ODS) : compréhension des relations microstructure / propriétés mécaniques; 2012, https://www.theses.fr/2012ENMP0052,
[16] M. Praud, F. Mompiou, J. Malaplate, J. Garnier, B. Fournier. Study of the deformation mechanisms in a Fe–14% Cr ODS alloy. Journal of Nuclear Materials 2012; 428:90-97., .
[17] Sheng-Yi Zhong, Joel Ribis, Nicolas Lochet, Vincent Klosek, Marie-Hélène Mathon. The Effect of Y/Ti Ratio on Oxide Precipitate Evolution in ODS Fe-14 Wt Pct Cr Alloys. Metallurgical and Materials Transactions A 2015; 46:1413-1418., .
[18] Gabriel Spartacus, Joël Malaplate, Frédéric De Geuser, Amélie Gangloff, Alexis Deschamps. Nano-oxide precipitation kinetics during the consolidation process of a ferritic oxide dispersion strengthened steel. Scripta Materialia 2020; 188:10-15., .
[19] H. Sakasegawa, L. Chaffron, F. Legendre, T. Cozzika, Y. de Carlan. Correlation between chemical composition and size of very small oxide particles in the MA957 ODS ferritic alloy. Journal of Nuclear Materials 2009; 384:115-118., .
[20] N. Sallez, C. Hatzoglou, F. Delabrouille, L. Chaffron, B. Radiguet, P. Donnadieu. Precipitates and boundaries interaction in ferritic ODS steels. Journal of Nuclear Materials 2016; 472:118-126., .
[21] M. Laurent-Brocq, F. Legendre, M-H. Mathon, S. Poissonnet, P. Pareige, O. Leseigneur. Influence of ball-milling and annealing conditions on nanocluster characteristics in oxide dispersion strengthened steels. Acta Materialia 2012; 60:7150-7159., .
[22] C. Hatzoglou, B. Radiguet, F. Vurpillot. A chemical composition correction model for nanoclusters observed by APT - Application to ODS steel nanoparticles. Journal of Nuclear Materials 2018; 505:240-248., .
[23] M. Loyer-Prost, J-S. Merot, J. Ribis, L. Chaffron. High resolution Transmission Electron Microscopy characterization of a milled oxide dispersion strengthened steel powder. Journal of Nuclear Materials 2016; 479:76-84., .
[24] S. Ohtsuka, J. Takekawa. Effect of Additions of B and Al2O3 Fine Powders on the Sintering of SKH51 Steel Powder. Journal of the Japan Society of Powder and Powder Metallurgy 2004; 51:27-30., .
[25] Cast3M21. http://www-cast3m.cea.fr/; 2021., .

[26] F. Nagase, T. Fuketa, T. Sugiyama. Optimized Ring Tensile Test Method and Hydrogen Effect on Mechanical Properties of Zircaloy Cladding in Hoop Direction. Journal of Nuclear Science and Technology 2009; 46:545-552., .
[27] T. Jaumier. Study of the tensile anisotropy of extruded ODS steel tubes using notched rings. 16th European Mechanics of Materials Conference 2018.,
[28] G. Sanyal, M. K. Samal. A geometry-dependent generalized shape function for calculation of stress intensity factor for axially cracked thin-walled tubes. International Journal of Advanced Structural Engineering 2014; 6:1-11., .
[29] A-M Alvarez Holston, J. Stjärnsäter. On the effect of temperature on the threshold stress intensity factor of delayed hydride cracking in light water reactor fuel cladding. Nuclear Engineering and Technology 2017; 49:663-667., .
[30] S. Cravero, C. Ruggieri. Estimation procedure of J-resistance curves for SE(T) fracture specimens using unloading compliance. Engineering Fracture Mechanics 2007; 74:2735-2757., .
[31] M.N. Vu, S. Geniaut, P. Massin. Numerical investigation on corner singularities in cracked plates using the G-theta method with an adapted θ field. Theoretical and Applied Fracture Mechanics 2015; 77:59-68., .
[32] C. Runge. Über empirische Funktionen und die Interpolation zwischen äquidistanten Ordinaten. Zeitschrift für Mathematik und Physik 1901; 46:224-243., .
[33] M.H. Sharobeam, J.D. Landes. The load separation criterion and methodology in ductile fracture mechanics. International Journal of Fracture 1991; 47:81–104., .
[34] M. H. Sharobeam, J. D. Landes. The load separation and η_pl. International Journal of Fracture 1993; 59:213–226., .
[35] P.C. Paris, H. Ernst, C.E. Turner. A J-Integral approach to Development of η-Factors. Fracture Mechanics: Twelfth Confirence 1980; 11:338- 351., .
[36] V. Grigoriev, B. Josefsson, A. Lind, B. Rosborg. Fracture Toughness of Zircaloy Cladding Tubes. ASTM STP 1295, Er Bradley, Gp Sabol, Editors. Zirconium in the Nuclear Industry: 11th International Symposium; 1995, p. 431-447.,
[37] H.A. Ernst, P.C. Paris. Techniques of Analysis of Load-Displacement Records by J-Integral Methods. Nuclear Regulatory Commission, NUREG/CR-1222 1980., .
[38] J. Besson, C.N. McCowan, E.S. Drexler. Modeling flat to slant fracture transition using the computational cell methodology. Engineering Fracture Mechanics 2013; 104:80-95., .
[39] S.A. El-Naaman, K.L. Nielsen. Observations on Mode I ductile tearing in sheet metals. European Journal of Mechanics - A/Solids 2013; 42:54-62, .